



Excitation of Ion Cyclotron Waves by Ion and Electron Beams in Compensated-current System

L. Xiang^{1,2}, D. J. Wu¹ , and L. Chen¹

¹ Purple Mountain Observatory, Chinese Academy of Sciences, 210008, Nanjing, People's Republic of China; djwu@pmo.ac.cn

² University of Science and Technology of China, 230026, Hefei, People's Republic of China

Received 2017 October 24; revised 2018 March 4; accepted 2018 March 11; published 2018 April 20

Abstract

Ion cyclotron waves (ICWs) can play important roles in the energization of plasma particles. Charged particle beams are ubiquitous in space, and astrophysical plasmas and can effectively lead to the generation of ICWs. Based on linear kinetic theory, we consider the excitation of ICWs by ion and electron beams in a compensated-current system. We also investigate the competition between reactive and kinetic instabilities. The results show that ion and electron beams both are capable of generating ICWs. For ICWs driven by ion beams, there is a critical beam velocity, v_{bi}^c , and critical wavenumber, k_z^c , for a fixed beam density; the reactive instability dominates the growth of ICWs when the ion-beam velocity $v_{bi} > v_{bi}^c$ and the wavenumber $k_z < k_z^c$, and the maximal growth rate is reached at $k_z \simeq 2k_z^c/3$ for a given $v_{bi} > v_{bi}^c$. For the slow ion beams with $v_{bi} < v_{bi}^c$, the kinetic instability can provide important growth rates of ICWs. On the other hand, ICWs driven by electron beams are excited only by the reactive instability, but require a critical velocity, $v_{be}^c \gg v_A$ (the Alfvén velocity). In addition, the comparison between the approximate analytical results based on the kinetic theory and the exact numerical calculation based on the fluid model demonstrates that the reactive instabilities can well agree quantitatively with the numerical results by the fluid model. Finally, some possible applications of the present results to ICWs observed in the solar wind are briefly discussed.

Key words: instabilities – solar wind – waves

1. Introduction

Ion cyclotron waves (ICWs) are a kind of left-hand polarized waves with frequencies below and near the ion cyclotron frequency (ω_{ci}) in the plasma frame (Gary 1993). They are the continuation of sheared Alfvén waves (AWs) at higher frequencies (near ω_{ci}), and they appear to be the circular (for parallel propagation) or elliptical (for oblique propagation) polarized waves associated with magnetic perturbation transverse to the background magnetic field (Zhao 2015). Because ICWs can play significant roles in the energy transfer between the wave and the ions through cyclotron resonance (Roberts & Li 2015), extensive theory and simulation studies in past decades revealed that ICWs are possibly associated with a variety of processes and phenomena in space and solar plasmas, such as generating electromagnetic ion cyclotron emissions and the anomalous resistivity in the auroral acceleration region (Ahrwar et al. 2007); preferential heating of ions in the solar corona (Mecheri 2013); ion heating through the wave-particle interaction in coronal hole (Mecheri & Marsch 2007; Isenberg & Vasquez 2011); and accelerating the electrons up to the relativistic velocity in coronal loops (Li et al. 1993). Meanwhile, a number of observations have also shown that ICWs exist ubiquitously in various plasma environments from laboratory plasma in Tokamak (Adam et al. 1978) to the ionosphere (Pilipenko et al. 2012), the magnetosphere (Roberts & Li 2015), the interplanetary medium (Fraser 1985; Siu-Tapia et al. 2015), and the solar wind (Jian et al. 2009, 2010; Zhao et al. 2017).

Charged particle beams, which are one of the most ubiquitous components in cosmic plasmas, can be encountered in various parts of space and astrophysical plasmas; for instance, in the auroral energetic electrons in the polar magnetosphere at an altitude of $1-2R_E$ (Earth radius)

(Wu 2012); in ion and electron beams in the ionosphere (Ahrwar et al. 2007; Zheng et al. 2012); in energetic electron beams in near-Earth reconnection regions (Åsnes et al. 2008); in energetic ion beams in the storm-time magnetosphere (Forster et al. 2013); in ion streams (Feldman et al. 1973; Tu et al. 2004); and in super-thermal ions (Feldman et al. 1974; Goodrich & Lazarus 1976) in the interplanetary solar wind, solar flaring-energetic ions and electrons in the solar atmosphere (Wu 2012), and various energetic cosmic rays from supernova blast waves and other astrophysical activities (Bell 2005). In particular, numerous observations from many satellites show that these ion and electron beams are frequently accompanied by ICW activities in space plasma, such as Van Allen Probe B in the magnetosphere (Khazanov et al. 2017), and Wind (Gary et al. 2016; Jian et al. 2016) in the solar wind. This indicates that the non-thermal charged particle beams possibly supply important driving energy sources to excite the ICW activities.

The excitation and generation mechanisms have been an increasingly interesting subject, with extensive observations in laboratories, space, and astrophysical plasmas. A variety of free energy can contribute to the generation of ICWs, such as temperature anisotropy with the perpendicular temperature larger than the parallel temperature (Gary et al. 1976, 1993); the loss-cone distribution for the electron and ion velocity distribution (Ahrwar et al. 2006); the combined loss-cone and temperature anisotropy distribution of suprathermal ions (Hua et al. 2011); and the perpendicular pickup ions (Russell & Blancocano 2007). In addition, the relative drift between different ion populations also may lead to the effective excitation of ICWs (Gary et al. 1985), and moreover Winske & Gary (1986) found that the instability driven by the drift of heavier ions has a larger growth rate. However, their discussion is just for non-resonant interaction, that is, the reactive

instability, which neglects the Landau damping effect. Unlike the kinetic instability due to the Landau damping effect of wave-particle resonance, the reactive instability is in nature the current bunching effect of charged particle streams via the wave electromagnetic field in the fluid model of plasma as a continuous medium (Bohm & Gross 1949).

In principle, a charged particle beam with appropriate parameters in plasmas may simultaneously excite the reactive and kinetic instabilities. On the other hand, when injected into the plasma, the charged particle beams also produce a return current to compensate the beam current in the way to maintain the compensated-current system in a quasi-neutral state in both charge and current (van den Oord 1990; Wu 2012). Some investigations showed that low-frequency (\ll the ion gyrofrequency) and high-frequency (near the ion gyrofrequency) kinetic AWs can both be excited by ion beams and currents, or by anisotropic particles distributions (Voitenko 1998; Voitenko & Goossens 2003). In particular, Malovichko et al. (2014, 2015) recently found that the compensated currents may effectively drive a new oblique Alfvénic instability in MHD scales, as well as the kinetic AW instability in kinetic scales. In this paper, we take into account the compensating effect of the return current in the beam-return current system, and study the reactive and kinetic instabilities of ICWs in the presence of ion and electron beams. The results show that although the ion and electron beams both can effectively excite ICW instability, their parametric properties have obvious differences. In particular, the reactive instability is significantly different from the kinetic instability. The results presented in this paper can be of potential importance for a better understanding of the excitation and generation mechanisms of ICWs, which are possibly associated with a variety of processes and phenomena in space and astrophysical plasmas.

This paper is organized as follows. First, based on the kinetic theory, the basic model of the compensated-current system and the dispersion relation of ICWs are derived in Section 2. Then, the reactive and kinetic instabilities by ion and electron beams; the comparison with the exact numerical calculations based on the fluid model; and some possible application to relative observations in the solar wind are discussed in Section 3. Finally, a summary and conclusion are presented in Section 4.

2. Basic Model of Compensated-current System and ICW Dispersion Relation

Consider a compensated-current system magnetized by a uniform background magnetic field \mathbf{B}_0 along the z axis, consisting of four components: the ion and electron beams with the number densities n_{bi} and n_{be} , and the beam velocities v_{bi} and v_{be} , respectively, propagating along the background magnetic field, the motionless background ions, and the background electrons with the drift velocity v_{de} , which provides the return current to compensate the ion/electron-beam current and to maintain the current neutrality in the plasma (van den Oord 1990). For all plasma components, the unperturbed distribution functions can be expressed by

(Voitenko & Goossens 2003)

$$f_{0s} = \frac{n_s}{(2\pi v_{Ts}^2)^{3/2}} \exp\left[-\frac{v_{\perp}^2}{2v_{Ts}^2} - \frac{(v_{\parallel} - v_s)^2}{2v_{Ts}^2}\right], \quad (1)$$

where $v_{Ts} = \sqrt{T_s/m_s}$, T_s , and m_s represent the thermal velocity, temperature, and mass for the s th species ($s = i, e, bi,$ and be), respectively, and n_s, q_s, v_s are the mean number density, charge, and velocity of the s th species. The subscripts \perp and z indicate directions perpendicular and parallel to the background magnetic field, respectively. Taking account of the charge-neutral condition $\sum_s q_s n_s = 0$ and the current-neutral condition $\sum_s q_s n_s v_s = 0$, the drift velocity of background electrons, v_{de} , is derived as follows:

$$v_{de} = \frac{n_{bi}v_{bi} - n_{be}v_{be}}{n_0 - n_{be}}. \quad (2)$$

The perturbed distribution function for the species s , f_{s1} , is governed by the following linearized Vlasov equation (Wu 2012):

$$\left[\frac{\partial}{\partial t} + \mathbf{v} \cdot \nabla + \frac{q_s}{m_s}(\mathbf{v} \times \mathbf{B}_0) \cdot \nabla_{\mathbf{v}}\right] f_{s1} = -\frac{q_s}{m_s}(\mathbf{E}_1 + \mathbf{v} \times \mathbf{B}_1) \cdot \nabla_{\mathbf{v}} f_{s0}, \quad (3)$$

where \mathbf{E}_1 and \mathbf{B}_1 represent the perturbed electric and magnetic fields, respectively, and ∇ and $\nabla_{\mathbf{v}}$ are the gradient operators in the position and velocity spaces, respectively.

For quasi-parallel propagating modes with the wave vector $\mathbf{k} = k_{\perp} \mathbf{e}_{\perp} + k_z \mathbf{e}_z$ ($k_{\perp} \ll k_z$), the kinetic dispersion relation for left-hand polarized waves can be written in following form (Aleksandrov et al. 1984):

$$\varepsilon_{xx} - i\varepsilon_{xy} = \left(\frac{ck_z}{\omega}\right)^2, \quad (4)$$

where the ε factors are the elements of the dielectric tensor and $k_{\perp} = k_x$ and $\mathbf{e}_{\perp} = \mathbf{e}_x$ have been used.

Substituting the unperturbed distribution function given by Equation (1) into Equation (3), the dielectric tensor elements can be derived from the standard analysis of linear Vlasov-Maxwell kinetic theory as follows (Lysak & Lotko 1996; Wu 2012):

$$\varepsilon_{xx} = 1 + \sum_s \frac{\omega_{ps}^2}{\omega^2} \xi_{s,0} \sum_{n=\pm 1} n^2 \frac{\Gamma_n(\lambda_s)}{\lambda_s} Z(\xi_{s,n}),$$

$$\varepsilon_{xy} = i \sum_s \frac{\omega_{ps}^2}{\omega^2} \xi_{s,0} \sum_{n=\pm 1} n \Gamma'_n(\lambda_s) Z(\xi_{s,n}), \quad (5)$$

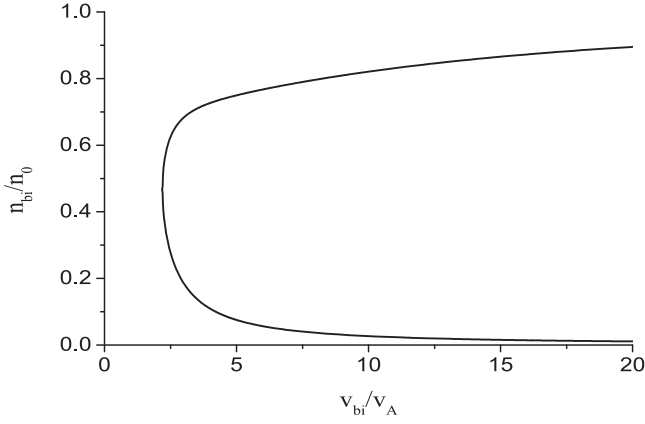


Figure 1. Beam density–velocity parametric regimes with (the right-hand side of the line) and without growth (the left-hand side of the line) for the reactive instability driven by ion beams, where the fixed parameters $\beta_e = 0.36$, $T_i/T_e = 1$, and $k_z \rho_i = 0.1$ have been used.

where

$$\begin{aligned} \Gamma_n(\lambda_s) &= I_n(\lambda_s) \exp(-\lambda_s), \quad \lambda_s = \frac{k_{\perp}^2 v_{Ts}^2}{\omega_{cs}^2}, \\ Z(\xi_{s,n}) &= \frac{1}{\pi} \int_{-\infty}^{+\infty} \frac{\exp(-t^2)}{t - \xi_{s,n}} dt, \\ \xi_{s,n} &= \frac{\omega - k_z v_s - n\omega_{cs}}{\sqrt{2} k_z v_{Ts}}, \quad \xi_{s,0} = \frac{\omega - k_z v_s}{\sqrt{2} k_z v_{Ts}}. \end{aligned} \quad (6)$$

In the above expressions, $I_n(\lambda_s)$ is the n -order modified-Bessel function of the first kind, $Z(\xi_{s,n})$ is the plasma dispersion function, ω_{ps} and ω_{cs} are the plasma oscillation frequency and Larmor gyrofrequency for the s th species, respectively.

Under warm beams, we assume $k_z v_{Tbi}/\omega_{ci} < 1$ and $k_z v_{Tbe}/\omega_{ce} \ll 1$. It is reasonable to employ the large-argument expansion for the plasma dispersion function Z with $n \neq 0$; consequently, the dispersion relation in Equation (4) reduces to the following form:

$$M \frac{\omega^2}{\omega_{ci}^2} + N \frac{\omega}{\omega_{ci}} - P = 0, \quad (7)$$

with the coefficients

$$\begin{aligned} M &= \frac{v_A^2}{c^2} - \frac{n_0 - n_{bi}}{n_0} A(\omega), \\ N &= -\frac{n_0 - n_{bi}}{n_0} A(\omega) + \frac{n_{bi}}{n_0} \frac{\omega_{ci}}{\sqrt{2} k_z v_{Tbi}} B(\omega) \\ &\quad - \frac{n_0 - n_{be}}{n_0} \frac{\omega_{ce}}{\sqrt{2} k_z v_{Te}} C(\omega) - \frac{n_{be}}{n_0} \frac{\omega_{ce}}{\sqrt{2} k_z v_{Tbe}} D(\omega), \\ P &= \frac{n_{bi}}{n_0} \frac{v_{bi}}{\sqrt{2} v_{Tbi}} B(\omega) - \frac{m_i}{m_e} \frac{n_{bi} v_{bi} - n_{be} v_{be}}{\sqrt{2} n_0 v_{Te}} C(\omega) \\ &\quad - \frac{m_i}{m_e} \frac{n_{be}}{n_0} \frac{v_{be}}{\sqrt{2} v_{Tbe}} D(\omega) + \frac{k_z^2 v_A^2}{\omega_{ci}^2}. \end{aligned} \quad (8)$$

To consider the effect of Landau damping in the process of wave-particle interaction, we should keep the imaginary terms in the plasma dispersion function of Z . In the above expansions (Equation (8)), the coefficients of $A(\omega)$, $B(\omega)$, $C(\omega)$, and $D(\omega)$ can be further expanded by Taylor series formula in the small parameter ω/ω_{ci} for the low-frequency case of $\omega < \omega_{ci}$ as follows:

$$\begin{aligned} A(\omega) &= A_0 + A_1 \frac{\omega}{\omega_{ci}}, \quad B(\omega) = B_0 + B_1 \frac{\omega}{\omega_{ci}} + B_2 \frac{\omega^2}{\omega_{ci}^2}, \\ C(\omega) &= C_0 + C_1 \frac{\omega}{\omega_{ci}} + C_2 \frac{\omega^2}{\omega_{ci}^2}, \\ D(\omega) &= D_0 + D_1 \frac{\omega}{\omega_{ci}} + D_2 \frac{\omega^2}{\omega_{ci}^2}, \end{aligned} \quad (9)$$

where the parameters A_0 to D_0 , A_1 to D_1 , and B_2 to D_2 are presented in the Appendix A.

By use of Equations (8) and (9), Equation (7) can be rewritten as

$$(M_r + iM_i) \frac{\omega^2}{\omega_{ci}^2} + (N_r + iN_i) \frac{\omega}{\omega_{ci}} - (P_r + iP_i) = 0, \quad (10)$$

where the parameters $M_{r(i)}$, $N_{r(i)}$, and $P_{r(i)}$ are given in the Appendix B.

Introducing the complex frequency $\omega = \omega_r + i\gamma$, the solution in Equation (10) leads to

$$\frac{\omega_r}{\omega_{ci}} = \frac{-M_r N_r - M_i N_i + \text{Re}[(M_r - iM_i) \sqrt{(N_r^2 - N_i^2 + 4M_r P_r) + i(2N_r N_i + 4M_r P_i)}]}{2(M_r^2 + M_i^2)}, \quad (11)$$

for the real frequency of the wave and

$$\frac{\gamma}{\omega_{ci}} = \frac{-M_r N_i + M_i N_r + \text{Im}[(M_r - iM_i) \sqrt{(N_r^2 - N_i^2 + 4M_r P_r) + i(2N_r N_i + 4M_r P_i)}]}{2(M_r^2 + M_i^2)}, \quad (12)$$

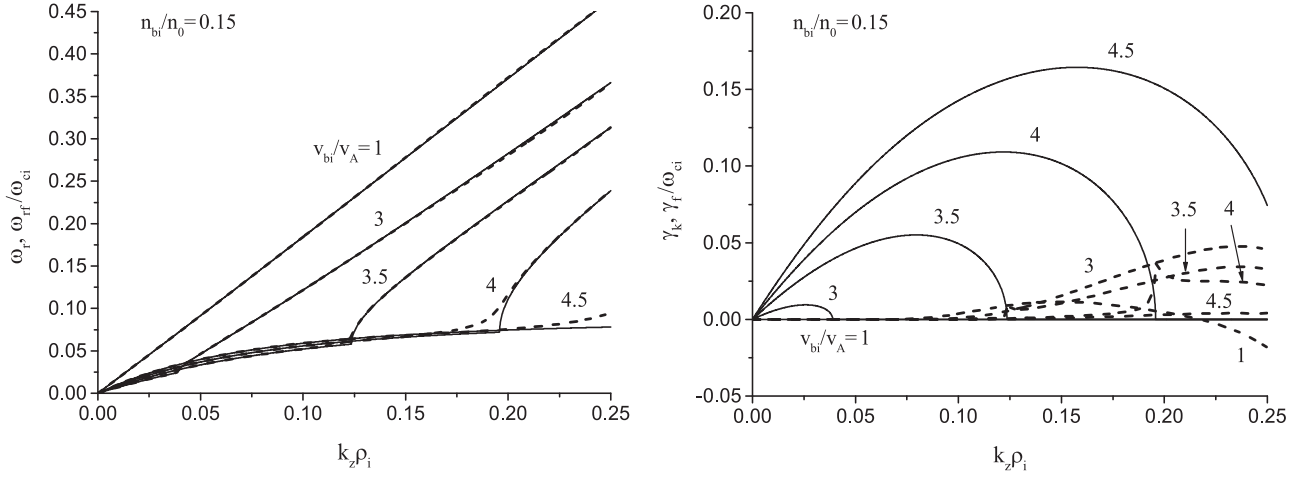


Figure 2. Normalized frequency (left) and growth rate (right) vs. the parallel wavenumber for the ion-beam density $n_{bi}/n_0 = 0.15$, where the lines correspond to the ion-beam velocity $v_{bi}/v_A = 1, 3, 3.5, 4,$ and 4.5 , respectively. In the left panel, the dashed and solid lines represent the dispersion relations with and without Landau damping, and in the right panel the dashed and solid lines represent the kinetic and reactive instabilities. The parameters $\beta_e = 0.36, T_i/T_e = 1,$ and $v_{Tbi}/v_{Ti} = 3.5$ have been used.

for the growth rate of the wave, where $\text{Re}[\dots]$ and $\text{Im}[\dots]$ represent the real and imaginary parts, respectively. Equation (11) describes the dispersion relation of ICWs in the compensated-current system including the effects of ion and electron beams. In particular, the dispersion relation of AWs, $\omega = k_z v_A$ (where $v_A = B_0/\sqrt{\mu_0 n_0 m_i}$ is the Alfvén velocity), can be recovered by omitting the effects of electron and ion beams as well as the Landau damping.

It should be noted that the dispersion relation of the parallel propagation actually has three modes (Aleksandrov et al. 1984): one pure longitudinal oscillation and two transverse ordinary (left-hand polarized) and extraordinary (right-hand polarized) waves. In the present work, however, we focus on the left-hand polarized waves, which become ICWs at higher frequencies near ω_{ci} and AWs at lower frequencies $\ll \omega_{ci}$. In addition, also we only concern the growing mode of ICWs with a positive growth rate (>0), and the damped mode with a negative growth rate has been neglected.

Ignoring the imaginary part of plasma dispersion function, Equations (11) and (12) give the real frequency and the growth rate of the reactive instability as

$$\frac{\omega_{rf}}{\omega_{ci}} = \frac{\text{Re}(\sqrt{N_r^2 + 4M_r P_r}) - N_r}{2M_r} \quad \text{and} \quad (13)$$

$$\frac{\gamma_f}{\omega_{ci}} = \frac{\text{Im}(\sqrt{N_r^2 + 4M_r P_r})}{2M_r},$$

respectively, which depends on plasma fluid parameters, such as the density, the flow velocity, and the thermal speed.

On the other hand, the growth rate of the kinetic instability can be obtained by the difference between Equations (12) and (13) as follows:

$$\frac{\gamma_k}{\omega_{ci}} = \frac{\gamma - \gamma_f}{\omega_{ci}}, \quad (14)$$

which is contributed by the imaginary part of plasma dispersion function and can be attributed to the effect of the wave-particle resonance.

3. Results and Discussion

Energetic ion beams are frequently observed in a variety of active phenomena in space and astrophysical plasmas (Goodrich & Lazarus 1976; Goldstein et al. 2000; Tu et al. 2004). In this section, we consider the instability driven by an ion beam in the compensated-current system; that is, the plasma consists of the motionless background ions, the drift background electrons, and the ion beam. Figure 1 shows the parametric regimes with and without the reactive instability in the $n_{bi}-v_{bi}$ parametric plane, where the line represents the critical line between the stable (the left-hand side) and unstable regimes (the right-hand side) for the fixed ratio of the electron pressure to the magnetic pressure $\beta_e = 0.36$, the ratio of the ion temperature to the electron temperature $T_i/T_e = 1$, and the parallel wavenumber $k_z \rho_i = 0.1$, where $\rho_i = v_{Ti}/\omega_{ci}$ is the ion gyroradius.

From Figure 1, it can be seen that the critical line is approximately symmetric about the beam density $n_{bi}/n_0 = 0.5$, because the case of $n_{bi}/n_0 > 0.5$ in the beam-comoving frame is equivalent to that of $n_{bi}/n_0 < 0.5$ in the background plasma frame. The critical ion-beam velocity (v_{bi}^c/v_A) increases as the beam density decreases in the regime of $n_{bi}/n_0 < 0.5$ or increases in the regime of $n_{bi}/n_0 > 0.5$. In particular, in the rather wide regime of $0.2 < n_{bi}/n_0 < 0.7$, the critical beam velocity ranges between $2 < v_{bi}^c/v_A < 3$; that is, a few times of the Alfvén velocity. This indicates that the condition for the reactive instability of $v_{bi} > v_{bi}^c$ is easily satisfied for major interesting cases in space and astrophysical plasmas.

Based on Equations (11) and (13), Figure 2 presents the real frequency (left), ω_r/ω_{ci} , and the growth rate (right), γ/ω_{ci} , versus the parallel wavenumber, $k_z \rho_i$, for the fixed ion-beam density $n_{bi}/n_0 = 0.15$ and the different ion-beam velocity $v_{bi}/v_A = 1, 3, 3.5, 4,$ and 4.5 , respectively. Similarly, Figure 3 shows the results for the fixed ion-beam velocity $v_{bi}/v_A = 3.8$ and the different ion-beam density $n_{bi}/n_0 = 0.05, 0.1, 0.13, 0.16,$ and 0.2 , respectively. The dashed lines in the right panels of Figures 2 and 3 represent the growth rates of the kinetic instability given by Equation (14) and the dashed lines in the left panels of Figures 2 and 3 do the real frequencies modified with the Landau damping. From Figures 2 and 3, one can find

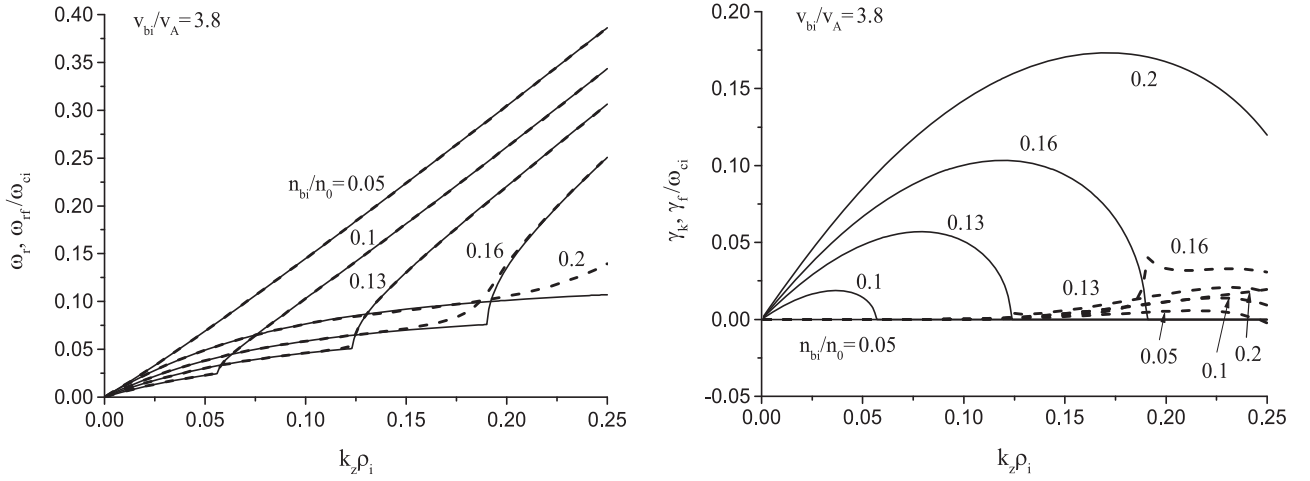


Figure 3. Normalized frequency (left) and growth rate (right) as a function of the normalized parallel wavenumber $k_z v_{Ti}/\omega_{ci}$ for the ion-beam velocity $v_{bi}/v_A = 3.8$, where the lines correspond to the ion-beam density $n_{bi}/n_0 = 0.05, 0.1, 0.13, 0.16$, and 0.2 , respectively. In the left panel, the dashed and solid lines represent the dispersion relations with and without Landau damping, and in the right panel the dashed and solid lines represent the kinetic and reactive instabilities. The plasma parameters are $\beta_e = 0.36$, $T_i/T_e = 1$, and $v_{Tbi}/v_{Ti} = 3.5$.

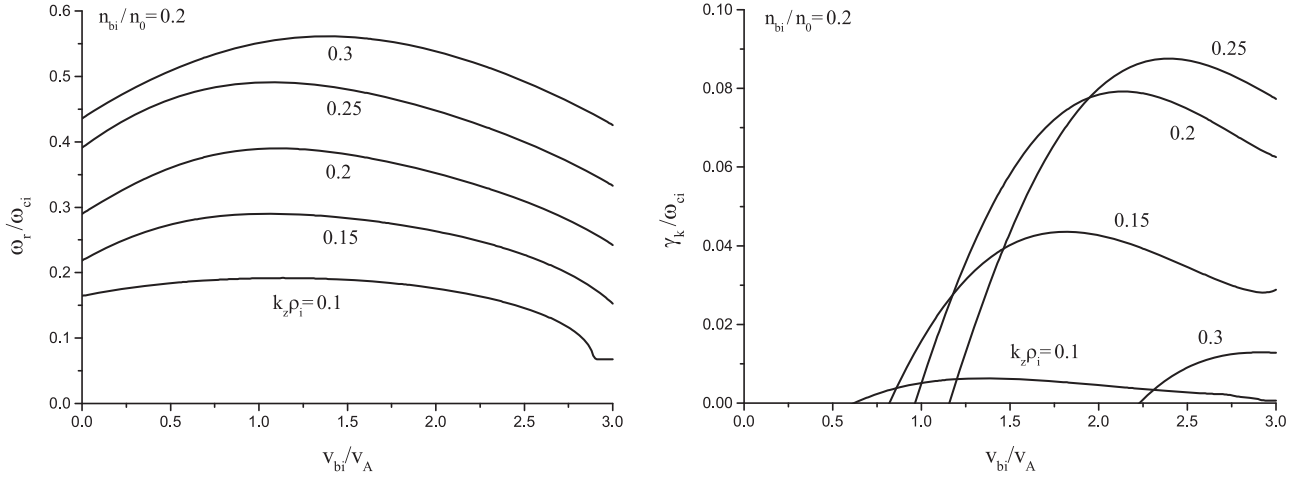


Figure 4. Normalized real frequency (left) and growth rate of the kinetic instability (right) vs. the ion-beam velocity for the fixed ion-beam density $n_{bi}/n_0 = 0.2$, where the lines correspond to the parallel wavenumber $k_z \rho_i = 0.1, 0.15, 0.2, 0.25$, and 0.3 , respectively. The plasma parameters $\beta_e = 0.36$, $T_i/T_e = 1$, and $v_{Tbi}/v_{Ti} = 3.5$ have been used.

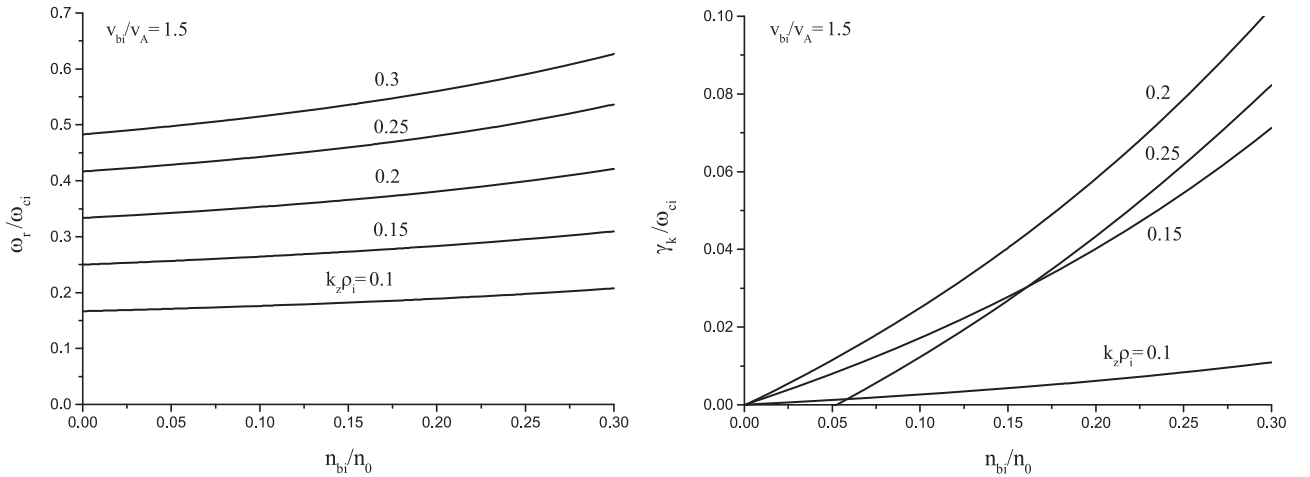


Figure 5. Normalized real frequency (left) and growth rate of the kinetic instability (right) vs. the ion-beam density for the fixed ion-beam velocity $v_{bi}/v_A = 1.5$, where the lines correspond to the parallel wavenumber $k_z \rho_i = 0.1, 0.15, 0.2, 0.25$, and 0.3 , respectively. The plasma parameters $\beta_e = 0.36$, $T_i/T_e = 1$, and $v_{Tbi}/v_{Ti} = 3.5$ have been used.

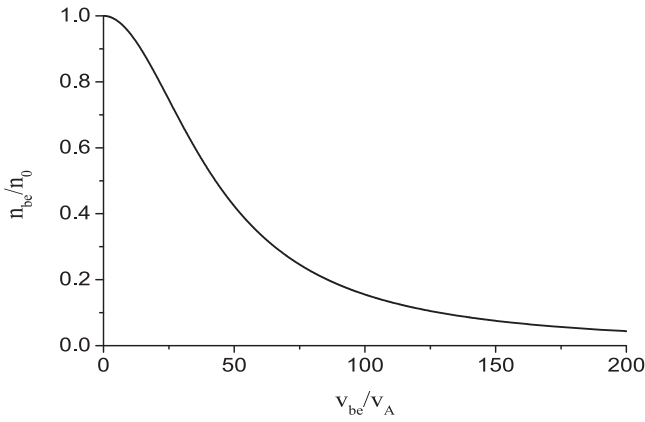


Figure 6. Beam density–velocity parametric regimes with (above the line) and without growth (below the line) for the reactive instability driven by electron beams, where the fixed parameter $T_i/T_e = 1$ has been used.

that there is a critical wavenumber k_z^c below that the reactive instability has a non-zero growth rate in the low wavenumber regime of $k_z < k_z^c$, implying the excitation of the reactive instability. In the higher wavenumber regime of $k_z > k_z^c$, the reactive instability does not work, but the kinetic instability has a non-zero growth rate and becomes the dominant excitation mechanism for ICWs.

Also, Figures 2 and 3 show that the reactive instability reaches its maximum at $k_z \approx 2k_z^c/3$; that is, the maximal growing wavenumber and that the critical wavenumber k_z^c and the growth rate of the reactive instability both increase as the density and velocity of the ion beam increases. This indicates that the ion beam with a larger velocity and higher density leads to a larger critical wavenumber and higher growth rate. In addition, Figures 2 and 3 show that so far as the ion-beam velocity exceeds the critical velocity of the reactive instability, v_{bi}^c , the reactive instability has a growth rate much higher than that of the kinetic instability because the latter is contributed by a fraction of particles, i.e., the resonant particles, and the former can be contributed by almost all particles in the plasma.

In general, however, the reactive instability has a high critical velocity v_{bi}^c above a few times of the Alfvén velocity v_A , as shown in Figure 1, while the kinetic instability has a lower critical velocity. Therefore, for the case of slow ion beams with a beam velocity below the critical velocity v_{bi}^c the kinetic instability will dominate the growth of ICWs. Based on Equations (11) and (14), Figures 4 and 5 give the real frequency and the kinetic growth rate versus the beam velocity and the beam density, respectively, for the slow ion beams with the beam velocity of a few times v_A , where Figure 4 is for a fixed beam density $n_{bi}/n_0 = 0.2$, Figure 5 is for a fixed beam velocity $v_{bi}/v_A = 1.5$, and the different lines correspond to the different wavenumbers $k_z\rho_i = 0.1, 0.15, 0.2, 0.25$, and 0.3 . From Figures 4 and 5, the real frequency of ICWs does not sensitively depend on the beam velocity and density, but increases obviously with the wavenumber $k_z\rho_i$ as shown in the left panels. The critical beam velocity of the kinetic instability increases with the wavenumber $k_z\rho_i$ for the fixed beam density as shown in the right panel of Figure 4. The right panel of Figure 4 shows that the kinetic instability has even a critical beam velocity lower than the local Alfvén velocity v_A for the low wavenumber ICWs of $k_z\rho_i < 0.2$ and that the maximal growth rate occurs in the beam velocity $1 < v_{bi}/v_A < 2.5$ for

the wavenumber $k_z\rho_i$ from 0.1 to 0.25. On the other hand, for the fixed beam velocity $v_{bi}/v_A = 1.5$ the right panel of Figure 5 shows that the kinetic growth rate γ_k increases with the beam density.

Energetic electron beams, which are a common and pervasive phenomenon in space and astrophysical plasmas, such as in the ionosphere (Zheng et al. 2012) and the magnetosphere (Åsnes et al. 2008), are one of the most important sources that drives plasma instabilities. This section discusses the instability driven by an electron beam in the compensated-current system, in which the plasma consists of the motionless background ions, the drift background electrons, and the electron beam.

Figure 6 presents the parametric regimes with and without the reactive instability in the n_{be} – v_{be} parametric plane for fixed parameter $T_i/T_e = 1$, where the regimes above and below the line correspond to with and without growth, respectively. From Figure 6, one can find that unlike the case of ion beams, the critical electron-beam velocity of the reactive instability, v_{be}^c/v_A , monotonically increases as the electron-beam density, n_{be}/n_0 , decreases. In particular, the critical velocity of the reactive instability driven by electron beams is much higher than that driven by ion beams for the cases of $n_{be}/n_0 < 0.5$. For instance, for the case of the beam density $n_{be}/n_0 = 0.3$ we have $v_{be}^c/v_A \approx 70$. This implies that it is more difficult to excite the ICW instability by electron beams than by ion beams.

Figures 7 and 8 present the real frequency (left) and growth rate (right) of ICWs versus the parallel wavenumber $k_z\rho_i$ for the case with the fixed beam density $n_{be}/n_0 = 0.25$ and the different beam velocity $v_{be}/v_A = 5, 70, 80, 90, 100$, and for the case with the fixed beam velocity $v_{be}/v_A = 90$ and the different beam density $n_{be}/n_0 = 0.05, 0.1, 0.2, 0.25$, and 0.35 , respectively, where other parameters $\beta_i = 0.36$, $T_i/T_e = 1$, and $v_{Tbe}/v_{Te} = 4$ have been used for the ratio of the ion pressure to the magnetic pressure, the ion to electron temperature ratio, and the thermal velocity ratio of the beam electrons to the background electrons, respectively. The dashed lines in the left and right panels represent the real frequency modified with the kinetic effect and the kinetic growth rate, respectively. Figures 7 and 8 both show that the growth rate of ICWs excited by the reactive instability driven by the electron beam monotonically increases with the wavenumber $k_z\rho_i$, and that the kinetic instability has a negative growth rate, implying the Landau damping of ICWs. These are considerably different from the results in the ion beam case presented in Figures 2 and 3. In addition, Figures 7 and 8 also show that growth rate increases with the electron-beam velocity as well as the electron-beam density.

Though the use of the dispersion relation solver based on the fluid model of plasmas (Xie 2014), the exact theoretical results of the growth rate of the reactive instability in the presence of ion and electron beams can be obtained via the numerical calculation. Figures 9 and 10 present the comparison between the preceding analytical approximation in Equation (13) and the exact numerical calculation for the ion-beam and electron-beam driven cases, respectively, where solid and dotted lines represent the growth rates given by the analytical approximation (γ_f) and the numerical calculation (γ_{fn}), respectively, and the parameters $T_i/T_e = 1$, $\beta_e = 0.64$ (Figure 9) and $\beta_i = 0.64$ (Figure 10) have been used. From Figures 9 and 10, as expected, the analytical approximation by Equation (13) (solid lines) can very well agree with the exact numerical

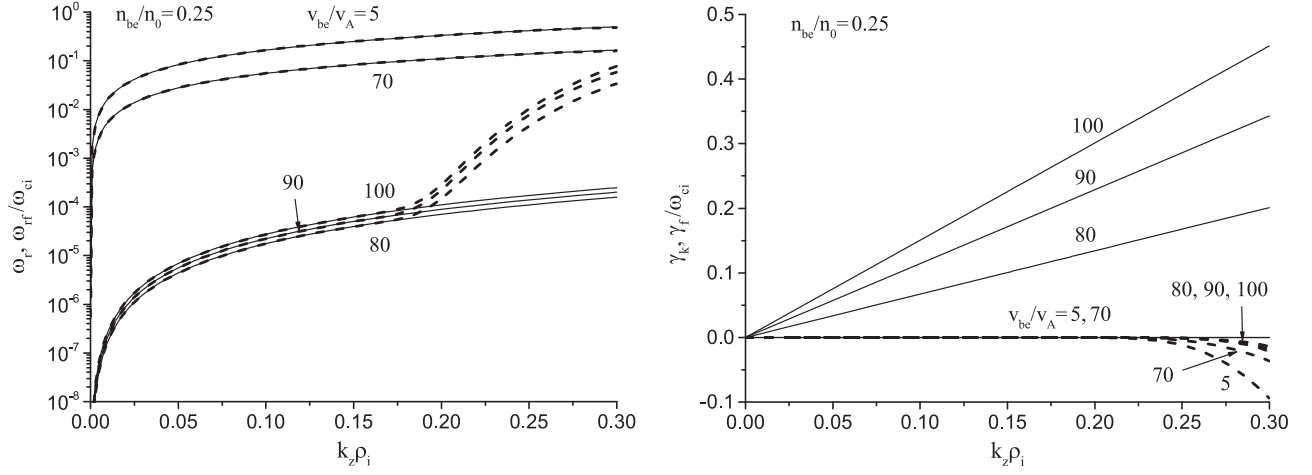


Figure 7. Variation of the dispersion relation (left) and growth rate (right) vs. the parallel wavenumber $k_z \rho_i$ for the electron-beam density $n_{be}/n_0 = 0.25$, where the lines correspond to the electron-beam velocity $v_{be}/v_A = 5, 70, 80, 90,$ and 100 , respectively. In the left panel, the dashed and solid lines represent the dispersion relations with and without the Landau damping, and in the right panel the dashed and solid lines represent the kinetic and reactive instabilities. Other parameters $\beta_i = 0.36, T_i/T_e = 1,$ and $v_{Tbe}/v_{Te} = 4$ have been used.

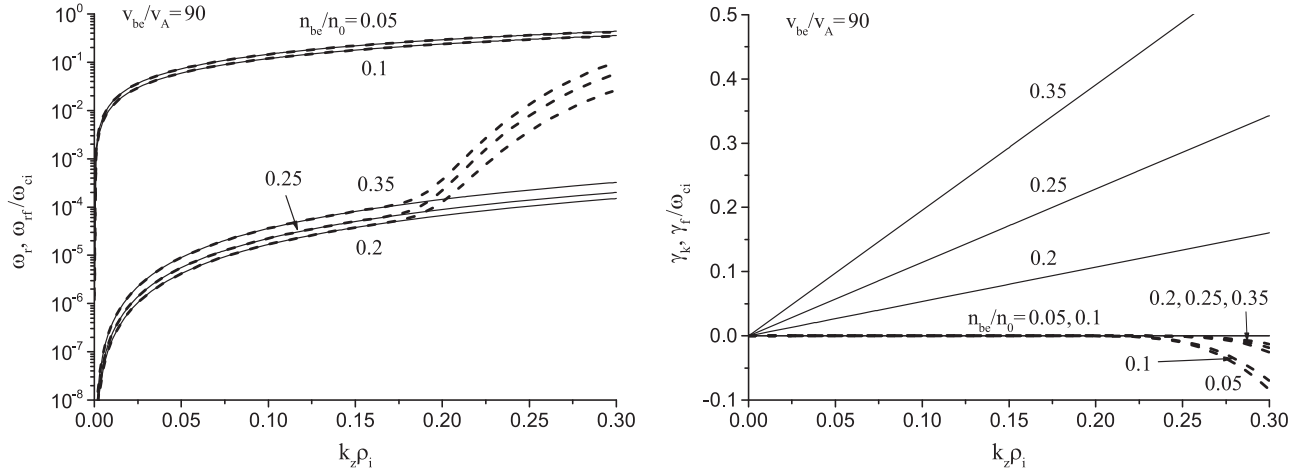


Figure 8. Plot of the dispersion relation (left) and growth rate (right) vs. the parallel wavenumber $k_z \rho_i$ for the electron-beam velocity $v_{be}/v_A = 90$, where the lines correspond to the electron-beam density $n_{be}/n_0 = 0.05, 0.1, 0.2, 0.25,$ and 0.35 , respectively. In the left panel, the dashed and solid lines represent the dispersion relations with and without the Landau damping, and in the right panel the dashed and solid lines represent the kinetic and reactive instabilities. Other parameters are $\beta_i = 0.36, T_i/T_e = 1,$ and $v_{Tbe}/v_{Te} = 4$.

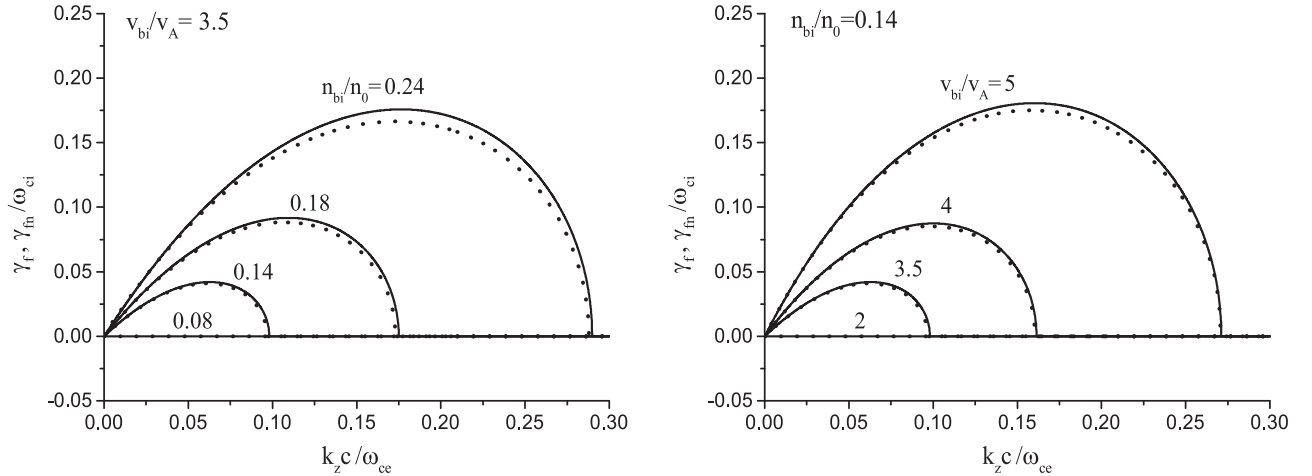


Figure 9. Comparison of the analytical results with the numerical calculation for the ion-beam driven case, where solid and dotted lines represent the analytical and numerical result, respectively, and the parameters $\beta_e = 0.64$ and $T_i/T_e = 1$ have been used.

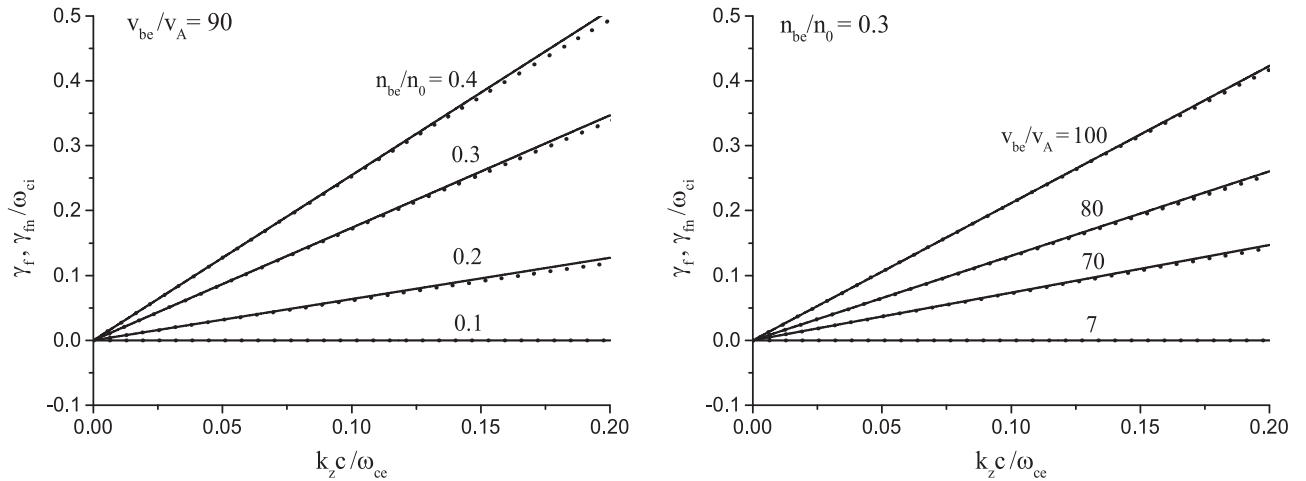


Figure 10. Comparison of the analytical results with the numerical calculation for the electron-beam driven case, where solid and dotted lines represent the analytical and numerical result, respectively, and the parameters $\beta_i = 0.64$ and $T_i/T_e = 1$ have been used.

results by the dispersion relation solver (dotted lines). Although some insignificant difference slowly and slightly increases with the beam density or velocity for the ion-beam driven case (Figure 9) and with the wavenumber k_z for the electron-beam driven case (Figure 10), they will not affect the analytic results presented in the preceding two sections, which are helpful for understanding some observational features in the solar wind.

Recently some typical events of enhanced magnetic fluctuations in the solar wind are identified as ICWs (Gary et al. 2016), in which the beam velocities for the six cases all are below twice v_A , implying that the reactive instability of ICWs does not work. However, the kinetic instability of ICWs presented in Figure 4 has a growth rate $\gamma_k \sim 2$ to $8 \times 10^{-2} \omega_{ci}$ for the ion-beam velocity $v_{bi} \sim 1$ to $2v_A$, and the typical parameters $n_{bi}/n_0 \sim 0.2$ and $k_z \rho_i \sim 0.2$, which is well higher than that of the temperature anisotropy with a typical value of $10^{-3} \sim 10^{-4} \omega_{ci}$ (Gary et al. 2016). This indicates that the kinetic instability of the ion beam possibly is responsible for the generation of the observed ICWs in the solar wind, although the reactive instability does not work.

4. Summary and Conclusion

In this paper, taking into account ion and electron beams, a general kinetic dispersion relation for ICWs in the compensated-current system is derived. Based on this dispersion relation, the competition between reactive and kinetic instabilities is investigated. The results show that the reactive instabilities of electron and ion beams both can lead to the development of the ICW instability. However, the reactive instability of ICWs driven by electron beams requires a very high critical velocity $v_{be}^c \gg v_A$ for the beam density $n_{be}/n_0 < 0.5$; moreover, the kinetic instability of electron beams entirely does not work. This indicates that it is very difficult to excite ICWs by electron beams.

On the other hand, the reactive and kinetic instabilities both can effectively excite ICWs. However, for the fast ion beam with the beam velocity larger than a few times of the Alfvén velocity, that is, $v_{bi} > v_{bi}^c \sim$ a few times of v_A , the reactive instability dominates the growth of ICWs in the wavenumber range of $0 < k_z < k_z^c$, where the growth rate reaches the maximum at $k_z \simeq 2k_z^c/3$, with a typical growth rate \sim one-tenth of the ion gyrofrequency. The corresponding critical wavenumber k_z^c and

the growth rate both increase with the density and velocity of the ion beam. While for the slow ion beam with the beam velocity $v_{bi} < v_{bi}^c$, the kinetic instability can be responsible for the growth of ICWs, but with a typical growth rate \sim several percent considerably lower than that of the reactive instability. The critical velocity of the kinetic instability decreases as the wavenumber decreases, and even lowers it to below the Alfvén velocity for the lower wavenumbers of $k_z \rho_i < 0.2$.

In addition, based on the dispersion relation solver (Xie 2014), the comparison between the exact numerical calculation to the approximate analytical result have been carried out to study the growth rate of the reactive instability in the presence of ion and electron beams. It is found that there is a very well agreement between the approximate analytical results given by the kinetic theory and the exact numerical calculations by the fluid model.

ICWs that are associated with ion and electron beams are ubiquitous in space and astrophysical plasmas (Jian et al. 2016; Khazanov et al. 2017). The present results can provide some reasonable explain for the existence of ICWs by the reactive instability of the fast ion beams or by the kinetic instability of the slow ion beams. For instance, the kinetic instability of the slow ion beams can be responsible for the events of enhanced magnetic fluctuations observed by Gary et al. (2016) in the solar wind, which are identified as ICWs, although the reactive instability of the ion beams does not work because where the ion-beam velocity is typically less than $2v_A$ (Goldstein et al. 2000; Tu et al. 2004). The present results can have some implications for understanding the presence of ICWs and the associated-ICW phenomena in space and astrophysical plasmas.

This work was supported by NSFC under grants 41531071, 11373070, and 41304136. The authors thank Drs. Q. H. Li, H. Y. Sun, and J. S. Zhao for their careful reading of the manuscript and their useful suggestions. We give a special thanks to the anonymous referee for the valuable suggestions and comments that helped improve the quality of this paper.

Appendix A Expressions of A, B, C, and D

With the help of Taylor series formula, the coefficients of A_0 to D_2 in Equation (9) can be given as follows:

$$\begin{aligned}
A_0 &= -1 - i\sqrt{\frac{\pi}{2}} \frac{\omega_{ci}}{k_z v_{Ti}} \exp\left(-\frac{\omega_{ci}^2}{2k_z^2 v_{Ti}^2}\right), \\
B_0 &= \frac{\sqrt{2}k_z v_{Tbi}}{k_z v_{bi} + \omega_{ci}} + i\sqrt{\pi} \exp\left[-\frac{(k_z v_{bi} + \omega_{ci})^2}{2k_z^2 v_{Tbi}^2}\right], \\
C_0 &= \frac{\sqrt{2}k_z v_{Te}}{k_z v_{de} + \omega_{ce}} + i\sqrt{\pi} \exp\left[-\frac{(k_z v_{de} + \omega_{ce})^2}{2k_z^2 v_{Te}^2}\right], \\
D_0 &= \frac{\sqrt{2}k_z v_{Tbe}}{k_z v_{be} + \omega_{ce}} + i\sqrt{\pi} \exp\left[-\frac{(k_z v_{be} + \omega_{ce})^2}{2k_z^2 v_{Tbe}^2}\right],
\end{aligned} \tag{15}$$

$$\begin{aligned}
A_1 &= i\sqrt{\frac{\pi}{2}} \frac{\omega_{ci}}{k_z v_{Ti}} \left(1 - \frac{\omega_{ci}^2}{k_z^2 v_{Ti}^2}\right) \exp\left(-\frac{\omega_{ci}^2}{2k_z^2 v_{Ti}^2}\right), \\
B_1 &= \frac{\sqrt{2}\omega_{ci}}{k_z v_{Tbi}} \left(\frac{k_z v_{Tbi}}{k_z v_{bi} + \omega_{ci}}\right)^2 + i\sqrt{\pi} \frac{\omega_{ci}}{k_z v_{Tbi}} \frac{k_z v_{bi} + \omega_{ci}}{k_z v_{Tbi}} \exp\left[-\frac{(k_z v_{bi} + \omega_{ci})^2}{2k_z^2 v_{Tbi}^2}\right], \\
C_1 &= \frac{\sqrt{2}\omega_{ci}}{k_z v_{Te}} \left(\frac{k_z v_{Te}}{k_z v_{de} + \omega_{ce}}\right)^2 + i\sqrt{\pi} \frac{\omega_{ci}}{k_z v_{Te}} \frac{k_z v_{de} + \omega_{ce}}{k_z v_{Te}} \exp\left[-\frac{(k_z v_{de} + \omega_{ce})^2}{2k_z^2 v_{Te}^2}\right], \\
D_1 &= \frac{\sqrt{2}\omega_{ci}}{k_z v_{Tbe}} \left(\frac{k_z v_{Tbe}}{k_z v_{be} + \omega_{ce}}\right)^2 + i\sqrt{\pi} \frac{\omega_{ci}}{k_z v_{Tbe}} \frac{k_z v_{be} + \omega_{ce}}{k_z v_{Tbe}} \exp\left[-\frac{(k_z v_{be} + \omega_{ce})^2}{2k_z^2 v_{Tbe}^2}\right],
\end{aligned} \tag{16}$$

and

$$\begin{aligned}
B_2 &= 2\sqrt{2} \left(\frac{\omega_{ci}}{k_z v_{Tbi}}\right)^2 \left(\frac{k_z v_{Tbi}}{k_z v_{bi} + \omega_{ci}}\right)^3 - i\sqrt{\pi} \left(\frac{\omega_{ci}}{k_z v_{Tbi}}\right)^2 \left[1 - \left(\frac{k_z v_{bi} + \omega_{ci}}{k_z v_{Tbi}}\right)^2\right] \exp\left[-\frac{(k_z v_{bi} + \omega_{ci})^2}{2k_z^2 v_{Tbi}^2}\right], \\
C_2 &= 2\sqrt{2} \left(\frac{\omega_{ci}}{k_z v_{Te}}\right)^2 \left(\frac{k_z v_{Te}}{k_z v_{de} + \omega_{ce}}\right)^3 - i\sqrt{\pi} \left(\frac{\omega_{ci}}{k_z v_{Te}}\right)^2 \left[1 - \left(\frac{k_z v_{de} + \omega_{ce}}{k_z v_{Te}}\right)^2\right] \exp\left[-\frac{(k_z v_{de} + \omega_{ce})^2}{2k_z^2 v_{Te}^2}\right], \\
D_2 &= 2\sqrt{2} \left(\frac{\omega_{ci}}{k_z v_{Tbe}}\right)^2 \left(\frac{k_z v_{Tbe}}{k_z v_{be} + \omega_{ce}}\right)^3 - i\sqrt{\pi} \left(\frac{\omega_{ci}}{k_z v_{Tbe}}\right)^2 \left[1 - \left(\frac{k_z v_{be} + \omega_{ce}}{k_z v_{Tbe}}\right)^2\right] \exp\left[-\frac{(k_z v_{be} + \omega_{ce})^2}{2k_z^2 v_{Tbe}^2}\right].
\end{aligned} \tag{17}$$

Appendix B Expressions of M, N, and P

Substituting Equations (8) and (9) into Equation (7), the coefficients in Equation (10) can be rewritten as follows:

$$\begin{aligned}
M_r &= \frac{n_0 - n_{bi}}{n_0} + \frac{n_{bi}}{n_0} \left(\frac{\omega_{ci}}{k_z v_{bi} + \omega_{ci}}\right)^2 - 2\frac{n_{bi}}{n_0} \frac{k_z v_{bi}}{\omega_{ci}} \left(\frac{\omega_{ci}}{k_z v_{bi} + \omega_{ci}}\right)^3, \\
N_r &= -\frac{n_{bi}}{n_0} + \frac{n_{bi}}{n_0} \frac{\omega_{ci}}{k_z v_{bi} + \omega_{ci}} - \frac{n_{bi}}{n_0} \frac{k_z v_{bi}}{\omega_{ci}} \left(\frac{\omega_{ci}}{k_z v_{bi} + \omega_{ci}}\right)^2 + 2\frac{n_{bi}}{n_0} \frac{m_e}{m_i} \frac{k_z v_{bi}}{\omega_{ci}} \\
&\quad - 2\frac{n_0 - n_{be}}{n_0} \left(\frac{m_e}{m_i}\right)^2 \left(\frac{k_z v_{de}}{\omega_{ci}}\right)^2 - 2\frac{n_{be}}{n_0} \left(\frac{m_e}{m_i}\right)^2 \left(\frac{k_z v_{be}}{\omega_{ci}}\right)^2, \\
P_r &= \frac{n_{bi}}{n_0} \frac{k_z v_{bi}}{k_z v_{bi} + \omega_{ci}} - \frac{n_{bi}}{n_0} \frac{k_z v_{bi}}{\omega_{ci}} + \frac{n_0 - n_{be}}{n_0} \frac{m_e}{m_i} \left(\frac{k_z v_{de}}{\omega_{ci}}\right)^2 + \frac{n_{be}}{n_0} \frac{m_e}{m_i} \left(\frac{k_z v_{be}}{\omega_{ci}}\right)^2 + \frac{k_z^2 v_A^2}{\omega_{ci}^2},
\end{aligned} \tag{18}$$

and

$$\begin{aligned}
M_i &= \sqrt{\frac{\pi}{2}} \frac{n_0 - n_{bi}}{n_0} \left(\frac{\omega_{ci}}{k_z v_{Ti}} \right)^3 \exp \left(-\frac{\omega_{ci}^2}{2k_z^2 v_{Ti}^2} \right) + \sqrt{\frac{\pi}{2}} \frac{n_{bi}}{n_0} \left(\frac{\omega_{ci}}{k_z v_{Tbi}} \right)^2 \frac{k_z v_{bi} + \omega_{ci}}{k_z v_{Tbi}} \exp \left[-\frac{(k_z v_{bi} + \omega_{ci})^2}{2k_z^2 v_{Tbi}^2} \right] \\
&+ \sqrt{\frac{\pi}{2}} \frac{n_{bi} v_{bi}}{n_0 v_{Tbi}} \left(\frac{\omega_{ci}}{k_z v_{Tbi}} \right)^2 \left[1 - \left(\frac{k_z v_{bi} + \omega_{ci}}{k_z v_{Tbi}} \right)^2 \right] \exp \left[-\frac{(k_z v_{bi} + \omega_{ci})^2}{2k_z^2 v_{Tbi}^2} \right] \\
&- \sqrt{\frac{\pi}{2}} \frac{n_{be} m_e}{n_0 m_i} \left(\frac{\omega_{ce}}{k_z v_{Tbe}} \right)^2 \frac{k_z v_{be} + \omega_{ce}}{k_z v_{Tbe}} \exp \left[-\frac{(k_z v_{be} + \omega_{ce})^2}{2k_z^2 v_{Tbe}^2} \right] \\
&- \sqrt{\frac{\pi}{2}} \frac{n_{be}}{n_0} \left(\frac{m_e}{m_i} \right)^2 \frac{k_z v_{be}}{\omega_{ci}} \left(\frac{\omega_{ce}}{k_z v_{Tbe}} \right)^3 \left[1 - \left(\frac{k_z v_{be} + \omega_{ce}}{k_z v_{Tbe}} \right)^2 \right] \exp \left[-\frac{(k_z v_{be} + \omega_{ce})^2}{2k_z^2 v_{Tbe}^2} \right] \\
&- \sqrt{\frac{\pi}{2}} \frac{n_0 - n_{be}}{n_0} \left(\frac{\omega_{ci}}{k_z v_{Te}} \right)^2 \frac{k_z v_{de} + \omega_{ce}}{k_z v_{Te}} \exp \left[-\frac{(k_z v_{de} + \omega_{ce})^2}{2k_z^2 v_{Te}^2} \right] \\
&- \sqrt{\frac{\pi}{2}} \frac{n_0 - n_{be}}{n_0} \left(\frac{m_e}{m_i} \right)^2 \frac{k_z v_{de}}{\omega_{ci}} \left(\frac{\omega_{ce}}{k_z v_{Te}} \right)^3 \left[1 - \left(\frac{k_z v_{de} + \omega_{ce}}{k_z v_{Te}} \right)^2 \right] \exp \left[-\frac{(k_z v_{de} + \omega_{ce})^2}{2k_z^2 v_{Te}^2} \right], \\
N_i &= \sqrt{\frac{\pi}{2}} \frac{n_0 - n_{bi}}{n_0} \frac{\omega_{ci}}{k_z v_{Ti}} \exp \left(-\frac{\omega_{ci}^2}{2k_z^2 v_{Ti}^2} \right) + \sqrt{\frac{\pi}{2}} \frac{n_{bi}}{n_0} \frac{\omega_{ci}}{k_z v_{Tbi}} \exp \left[-\frac{(k_z v_{bi} + \omega_{ci})^2}{2k_z^2 v_{Tbi}^2} \right] \\
&- \sqrt{\frac{\pi}{2}} \frac{n_{bi} v_{bi}}{n_0 v_{Tbi}} \frac{\omega_{ci}}{k_z v_{Tbi}} \frac{k_z v_{bi} + \omega_{ci}}{k_z v_{Tbi}} \exp \left[-\frac{(k_z v_{bi} + \omega_{ci})^2}{2k_z^2 v_{Tbi}^2} \right] - \sqrt{\frac{\pi}{2}} \frac{n_0 - n_{be}}{n_0} \frac{\omega_{ce}}{k_z v_{Te}} \exp \left[-\frac{(k_z v_{de} + \omega_{ce})^2}{2k_z^2 v_{Te}^2} \right] \\
&+ \sqrt{\frac{\pi}{2}} \frac{n_0 - n_{be} m_e}{n_0 m_i} \frac{k_z v_{de}}{\omega_{ci}} \left(\frac{\omega_{ce}}{k_z v_{Te}} \right)^2 \frac{k_z v_{de} + \omega_{ce}}{k_z v_{Te}} \exp \left[-\frac{(k_z v_{de} + \omega_{ce})^2}{2k_z^2 v_{Te}^2} \right] - \sqrt{\frac{\pi}{2}} \frac{n_{be}}{n_0} \frac{\omega_{ce}}{k_z v_{Tbe}} \exp \left[-\frac{(k_z v_{be} + \omega_{ce})^2}{2k_z^2 v_{Tbe}^2} \right] \\
&+ \sqrt{\frac{\pi}{2}} \frac{n_{be} m_e}{n_0 m_i} \frac{k_z v_{be}}{\omega_{ci}} \left(\frac{\omega_{ce}}{k_z v_{Tbe}} \right)^2 \frac{k_z v_{be} + \omega_{ce}}{k_z v_{Tbe}} \exp \left[-\frac{(k_z v_{be} + \omega_{ce})^2}{2k_z^2 v_{Tbe}^2} \right], \\
P_i &= \sqrt{\frac{\pi}{2}} \frac{n_{bi} v_{bi}}{n_0 v_{Tbi}} \exp \left[-\frac{(k_z v_{bi} + \omega_{ci})^2}{2k_z^2 v_{Tbi}^2} \right] - \sqrt{\frac{\pi}{2}} \frac{n_{be} k_z v_{be}}{n_0 \omega_{ci}} \frac{\omega_{ce}}{k_z v_{Tbe}} \exp \left[-\frac{(k_z v_{be} + \omega_{ce})^2}{2k_z^2 v_{Tbe}^2} \right] \\
&- \sqrt{\frac{\pi}{2}} \frac{n_0 - n_{be}}{n_0} \frac{k_z v_{de}}{\omega_{ci}} \frac{\omega_{ce}}{k_z v_{Te}} \exp \left[-\frac{(k_z v_{de} + \omega_{ce})^2}{2k_z^2 v_{Te}^2} \right]. \tag{19}
\end{aligned}$$

ORCID iDs

D. J. Wu  <https://orcid.org/0000-0001-8058-2765>

References

- Adam, J., Bonnal, J. F., Bresson, A., et al. 1978, *PhRvL*, **41**, 113
- Ahirwar, G., Varma, P., & Tiwari, M. S. 2006, *AnGeo*, **24**, 1919
- Ahirwar, G., Varma, P., & Tiwari, M. S. 2007, *AnGeo*, **25**, 557
- Aleksandrov, A. F., Bogdankevich, L. S., & Rukhadze, A. A. 1984, *Principles of Plasma Electrodynamics* (Berlin: Springer)
- Åsnes, A., Taylor, M. G. G. T., Borg, A. L., et al. 2008, *JGRA*, **113**, A07S30
- Bell, A. R. 2005, *MNRAS*, **358**, 181
- Bohm, D., & Gross, E. P. 1949, *PhRv*, **75**, 1851
- Feldman, W. C., Asbridge, J. R., Bame, S. J., & Montgomery, M. D. 1973, *JGR*, **78**, 6451
- Feldman, W. C., Asbridge, J. R., Bame, S. J., & Montgomery, M. D. 1974, *RvGSP*, **12**, 715
- Forster, D. R., Denton, M. H., Grande, M., & Perry, C. H. 2013, *JGRA*, **118**, A066
- Fraser, B. J. 1985, *SSRv*, **42**, 357
- Gary, S. P. 1993, *Theory of Space Plasma Microinstabilities* (Cambridge: Cambridge Univ. Press)
- Gary, S. P., Fuselier, S. A., & Anderson, B. J. 1993, *JGR*, **98**, 1481
- Gary, S. P., Jian, L. K., Broiles, T. W., et al. 2016, *JGRA*, **121**, 30
- Gary, S. P., Madland, C. D., & Tsurutani, B. T. 1985, *PhFI*, **28**, 3691
- Gary, S. P., Montgomery, M. D., Feldman, W. C., & Forslund, D. W. 1976, *JGR*, **81**, 1241
- Goldstein, B. E., Neugebauer, M., Zhang, L. D., & Gary, S. P. 2000, *GeoRL*, **27**, 53
- Goodrich, C. C., & Lazarus, A. J. 1976, *JGR*, **81**, 2750
- Hua, Y. P., Wu, D. J., & Wang, D. Y. 2011, *ChSBu*, **56**, 257
- Isenberg, P. A., & Vasquez, B. J. 2011, *ApJ*, **731**, 88
- Jian, L. K., Moya, P. S., Viñas, A. F., & Stevens, M. 2016, in *AIP Conf. Proc., Solar Wind*, ed. K. T. Das, B. Kristiawan, & M. S. Shekhawat (Melville, NY: AIP), 040007
- Jian, L. K., Russell, C. T., Luhmann, J. G., et al. 2009, *ApJL*, **701**, L105
- Jian, L. K., Russell, C. T., Luhmann, J. G., et al. 2010, *JGRA*, **115**, A12115
- Khazanov, G. V., Boardsen, S., Krivorutsky, E. N., et al. 2017, *JGRA*, **122**, 449
- Li, D., Wand, D., Tsai, S., Xu, M., & Mao, D. 1993, *SoPh*, **143**, 235
- Lysak, R. L., & Lotko, W. 1996, *JGR*, **101**, 5085
- Malovichko, P., Voitenko, Y., & De Keyser, J. 2014, *ApJ*, **780**, 175
- Malovichko, P., Voitenko, Y., & De Keyser, J. 2015, *MNRAS*, **452**, 4236

- Mecheri, R. 2013, [SoPh](#), **282**, 133
- Mecheri, R., & Marsch, E. 2007, [A&A](#), **474**, 609
- Pilipenko, V. A., Polozova, T. L., & Engebretson, M. 2012, [CosRe](#), **50**, 329
- Roberts, O. W., & Li, X. 2015, [ApJ](#), **802**, 1
- Russell, C., & Blancocano, X. 2007, [JASTP](#), **69**, 1723
- Siu-Tapia, A., Blanco-Cano, X., Kajdic, P., et al. 2015, [JGRA](#), **120**, 2363
- Tu, C.-Y., Marsch, E., & Qin, Z.-R. 2004, [JGRA](#), **109**, A05101
- van den Oord, G. H. J. 1990, [A&A](#), **234**, 496
- Voitenko, Y., & Goossens, M. 2003, [SSRv](#), **107**, 387
- Voitenko, Y. M. 1998, [SoPh](#), **182**, 411
- Winske, D., & Gary, S. P. 1986, [JGR](#), **91**, 6825
- Wu, D. J. 2012, *Kinetic Alfvén Wave: Theory, Experiment, and Application* (2nd ed.; Beijing: Science Press)
- Xie, H.-s. 2014, [CoPhC](#), **185**, 670
- Zhao, G. Q., Chu, Y. H., Lin, P. H., et al. 2017, [JGRA](#), **122**, 4879
- Zhao, J. 2015, [PhPI](#), **22**, 042115
- Zheng, H., Fu, S. Y., Zong, Q. G., et al. 2012, [PhRvL](#), **109**, 205001